

Electrical Control of Excitons in Bare-MoSe₂ and MoSe₂/NbSe₂ Heterostructure

Atanu Patra,^{1,*} Vishakha Kaushik,¹ Ali Sepas,² Subhamoy Sahoo,¹ Mathias Federolf,¹
Christian G. Mayer,^{1,3} Sebastian Klemmt,^{1,3} Monika Emmerling,¹ Simon Betzold,¹ Seth
Ariel Tongay,⁴ Fabian Hartmann,¹ Thomas Garm Pedersen,^{2,†} and Sven Höfiling^{1,3,‡}

¹*Julius-Maximilians-Universität Würzburg, Physikalisches Institut,*

Lehrstuhl für Technische Physik, Am Hubland, 97074 Würzburg, Germany

²*Department of Materials and Production, Aalborg University, DK-9220 Aalborg Øst, Denmark*

³*Physikalisches Institut and Würzburg-Dresden Cluster of Excellence ct.qmat, Germany*

⁴*Materials Science and Engineering, School for Engineering of Matter,*

Transport and Energy, Arizona State University, Tempe, 85287 Arizona, United States

Monolayer transition metal dichalcogenides (TMDCs) are promising materials for next-generation optoelectronic devices, owing to their strong excitonic responses and atomic thickness. Controlling their light emission electrically is a crucial step towards realizing practical nanoscale optoelectronic devices such as light-emitting diodes and optical modulators. However, photoluminescence (PL) quenching in van der Waals TMDC/metal heterostructures, caused by ultrafast interlayer charge or energy transfer, impedes such electrical modulation. Here, we investigate monolayer-MoSe₂/bulk-NbSe₂ heterostructures and demonstrate that a vertical electric field can effectively recover the PL intensity up to $\sim 80\%$ of bare-MoSe₂. Furthermore, our analysis reveals that the room temperature PL intensity can be tuned by nearly three orders of magnitude in bare-MoSe₂ and by about one order of magnitude in MoSe₂/NbSe₂ heterostructures. First-principles calculations incorporating spin-orbit coupling reveal that the perpendicular electric fields drive a transition from a direct to an indirect bandgap, fundamentally altering the optical response in the heterostructure. Unlike bare-MoSe₂, the heterostructure exhibits a pronounced thermal dependence of the enhancement factor, implying that exciton lifetime dominates over interfacial transfer processes. Our findings demonstrate reversible, electric-field-driven PL control at a TMDC/metal interface, providing a pathway to electrically tunable light emission and improved contact engineering in two-dimensional optoelectronic devices.

Keywords: MoSe₂/NbSe₂, vdW heterostructure, photoluminescence, electrical control, temperature dependence

I. INTRODUCTION

Van der Waals (vdW) heterostructures of transition metal dichalcogenides (TMDCs) materials have enabled the creation of artificial systems with novel functionalities that do not exist in nature. These include Moiré superlattices arising from controlled twisting or lattice mismatch, allowing for the exploration of emergent, strongly correlated electronic phases [1–5]. Furthermore, vdW stacking enables tunable type-I and type-II band alignment through the selection of material combination, stacking angle, and interlayer coupling [6, 7]. They also facilitate the realization of

* atanu.patra@uni-wuerzburg.de

† tgp@mp.aau.dk

‡ sven.hoeftling@uni-wuerzburg.de

long-lived interlayer excitons [8] with spatially separate charge carriers, distinct from the ultrafast recombination seen in monolayers [9, 10]. Such features are promising for advanced optoelectronic and excitonic device platforms [11–13].

However, the integration of TMDCs into devices remains challenging due to the high contact resistance at the TMDC/metal interface. Although graphene is widely used as a transparent electrode, its strong interlayer coupling with TMDCs induces significant interfacial charge and energy transfer, resulting in severe photoluminescence (PL) quenching [14, 15]. Moreover, work function mismatch between metal contacts and semiconducting TMDCs further contributes to high contact resistance [16], thereby constraining device performance. These limitations necessitate the exploration of alternative layered metals that offer better electronic compatibility. A highly interesting candidate is the layered two-dimensional (2D) metal NbSe₂, which is a type-II superconductor at temperatures below 8 K and metallic at higher temperatures with coexisting charge density wave order around 32 K [17]. Recent studies have shown the integration of 2D semiconducting layers into heterostructures with 2D NbSe₂ providing a platform for the manipulation of electronic and excitonic properties [18], and for the development of device applications, such as self-powered photodetectors [19]. In these devices, the dynamic tuning of optical properties is essential, enabling real-time control over excitonic behavior and light–matter interactions, which is critical for developing next-generation programmable and tunable optoelectronic functionalities using 2D materials [20].

In recent years, electrostatic gating offers a non-invasive approach to precisely tune optical properties in TMDCs [6]. This control enables modulation of quasiparticle bandgaps [21], phase transitions [22, 23], and symmetry-breaking phenomena [24, 25], as well as excitonic states [26–28], all without introducing structural disorder, unlike chemical doping. Vertical electric fields also alter hybrid excitons with strong dipolar interactions in TMDC bilayers [29–31]. Moreover, a recent study predicts that electric fields can modulate band alignment and Schottky barrier heights at TMDC/metal interfaces [32], a key factor in minimizing contact resistance and enhancing device performance. Building on these studies, understanding how vertical electric fields govern excitonic behavior and interfacial charge dynamics in TMDC/2D-metal heterostructures, especially under varying thermal conditions, remains largely unexplored.

In this work, we leverage vertical electric field modulation to investigate the PL properties in monolayer (ML)-MoSe₂/bulk-NbSe₂ (TMDC/metal) heterostructure. Measurements were performed at two positions, namely, bare-MoSe₂ (‘off’ position) and the MoSe₂/NbSe₂ heterostructure (‘on’ position). At room temperature ($T = 295$ K), the PL emission at the ‘on’ position is reduced by more than an order of magnitude compared to the ‘off’ position. Our results reveal that the direction of the electric field determines the PL enhancement in bare-MoSe₂ and MoSe₂/NbSe₂ heterostructure with a different degree of enhancement. Notably, at the ‘on’ position, the PL enhancement factor decreases with lowering temperature, while it remains nearly constant at the ‘off’ position. All measurements in this work were carried out down to $T = 20$ K, with a specific focus on the normal (non-superconducting) metallic regime of NbSe₂. Analytical calculations estimate that the electric field modifies the excitonic oscillator strength by altering the electron-hole (e - h) wavefunction overlap for the ‘off’ position. However, first-principle calculations on the MoSe₂/NbSe₂ heterostructure, representing the ‘on’ position, demonstrate that the field modifies the nature of the bandgap. Consequently, controlling the electric field allows modulation of the PL intensity and can recover emission at the ‘on’ position by up to $\sim 80\%$ of the ‘off’ position.

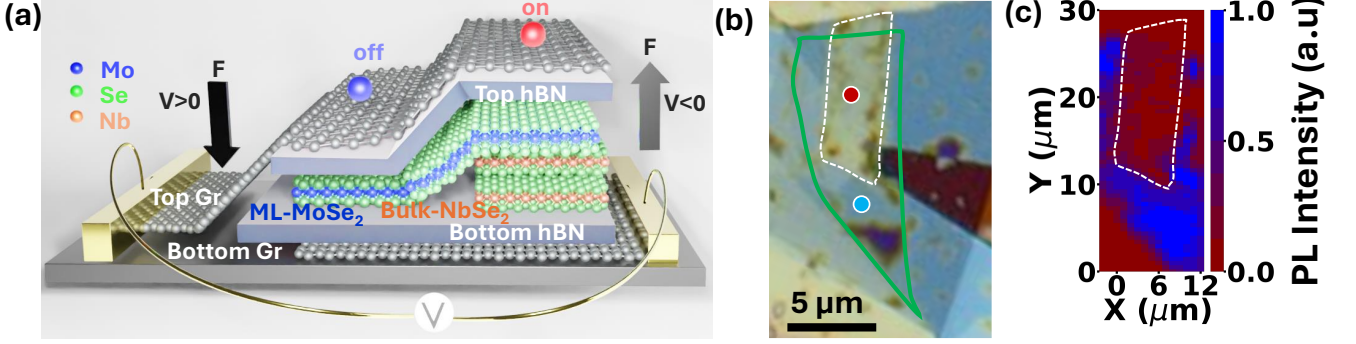


FIG. 1. (a) Schematic diagram and (b) optical image of a typical ML-MoSe₂/bulk-NbSe₂ heterostructure with top and bottom few-layer graphene contacts. (c) PL intensity map resulting from ML-MoSe₂ at room temperature ($T = 295$ K).

II. RESULTS

PL quenching in MoSe₂/NbSe₂ heterostructure

A schematic and optical micrograph of a typical MoSe₂/NbSe₂ stacked heterostructure, comprising ML-MoSe₂ interfaced with bulk NbSe₂, are shown in Fig. 1a and b, respectively. The thicknesses of MoSe₂ and NbSe₂ layers are determined by the optical contrast and Raman measurement, as shown in Supplementary Fig. S1. The heterostructure, marked by a white contour in Fig. 1b, is formed in the overlapping region of the two constituent materials. Note that the layers were not rotationally aligned, implying weak electronic hybridization between the incommensurate semiconducting and metallic layers. To study the effect of electric fields in the heterostructure, a capacitive structure is assembled on a pre-patterned gold electrode (details given in Supplementary section) using a layer-by-layer dry transfer stacking technique with hexagonal boron nitride (hBN) as the dielectric layer. The stack consists of few-layer-graphene/hBN/NbSe₂/MoSe₂/hBN/few-layer-graphene, with both the top and bottom hBN layers measuring approximately 12 ± 3 nm in thickness. The spatial PL intensity map, as shown in Fig. 1c, predominantly displays two colors. The blue colored area corresponds to bare-MoSe₂, while the region outlined by the white contour, representing the MoSe₂/NbSe₂ heterostructure, appears similar in color to the background. This indicates substantial PL quenching of MoSe₂ across the entire heterostructure area involving NbSe₂.

For simplicity, further analysis focuses on two representative positions, denoted as ‘off’ and ‘on’ in Fig. 1a by blue and red points, respectively. At $T = 295$ K, PL spectra in the absence of a vertical electric field (i.e., voltage, $V = 0$ V) at these two positions are presented in Fig. 2a and b, respectively. The spectra were fitted with two Gaussian functions representing the A-exciton and trion at 1.57 ± 0.05 eV and 1.53 ± 0.05 eV, respectively. The reflectance contrast spectra, $\Delta R/R = \frac{R-R_0}{R_0}$, where R and R_0 are the reflectance signal of the stack, with and without MoSe₂, respectively, for both ‘off’ and ‘on’ positions, are shown in Fig. 2c and d, respectively. The ‘off’-position spectrum predominantly indicates the real component of the dielectric function, while the ‘on’-position is governed by both real and imaginary parts [33]. The transition energies for the respective positions are marked by dotted lines in the figure. Although excitons in ML-MoSe₂ are spatially confined within the layer, the associated dipolar electric fields naturally extend beyond the layer due to the reduced dimensionality. As a result, forming a heterostructure of MoSe₂ with

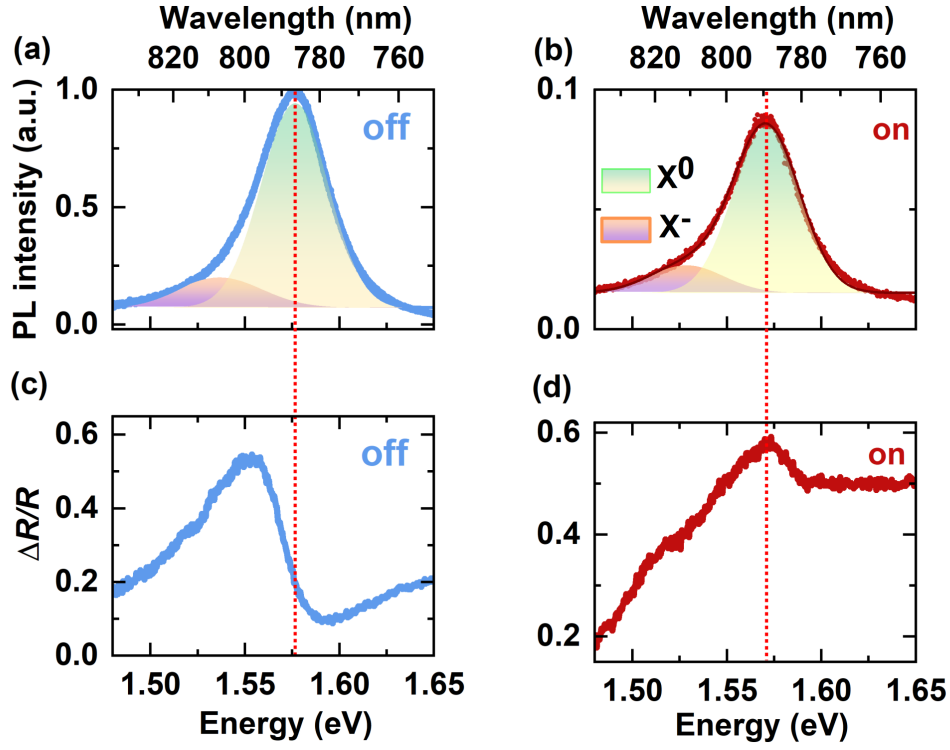


FIG. 2. (a) and (b) PL spectra at $T = 295$ K measured at the ‘off’ and ‘on’ positions, respectively, revealing a one order of magnitude reduction in intensity at the ‘on’ position compared to the ‘off’ position. (c) and (d) Corresponding reflectance contrast ($\Delta R/R$) spectra measured at the same points and at the same temperature.

metallic NbSe₂ inherently influences the excitonic behavior by enhancing environmental screening and modifying the local dielectric landscape. This interaction significantly alters the optical response, manifesting as distinct variations in $\Delta R/R$ at these two positions.

The most striking feature is the PL intensity suppression of around one order of magnitude (~ 11) between ‘off’ and ‘on’ positions. We conducted the measurements using a 532 nm laser at ~ 15 μ W power to ensure operation within the linear excitonic regime, as illustrated in Fig. S2a. Notably, the quenching factor remains consistent across the experimental power range as depicted in Fig. S2b. This quenching phenomenon is consistent with observations at semiconductor/metal interfaces, such as TMDC/graphene heterostructures, where PL intensity is suppressed due to photoinduced charge or energy transfer via Dexter or Förster processes [34]. This indicates substantial PL quenching of MoSe₂ across the entire heterostructure area involving NbSe₂. These processes occur on sub-picosecond timescales, significantly faster than the nanosecond-scale exciton lifetime at $T = 295$ K. The extent of PL quenching is strongly influenced by interlayer coupling, including factors such as interlayer distance, stacking sequence, and dielectric screening [14]. Since this quenching reflects a reduction in the exciton density, external electric fields that modulate exciton formation and recombination dynamics provide a promising route to restore or enhance PL emission in vdW heterostructures.

Electric field-dependent PL enhancement at room temperature

We next investigated the influence of an applied electric field (F) on the excitonic behavior, particularly, its effect on spectral intensity, as a proof-of-concept for implementing field-driven tunability in 2D materials-based heterostructures. A positive voltage ($V > 0$) corresponds to the top electrode near the MoSe₂ being positively biased while the bottom electrode remains grounded, resulting in a downward-pointing electric field, as illustrated in Fig. 1a. In

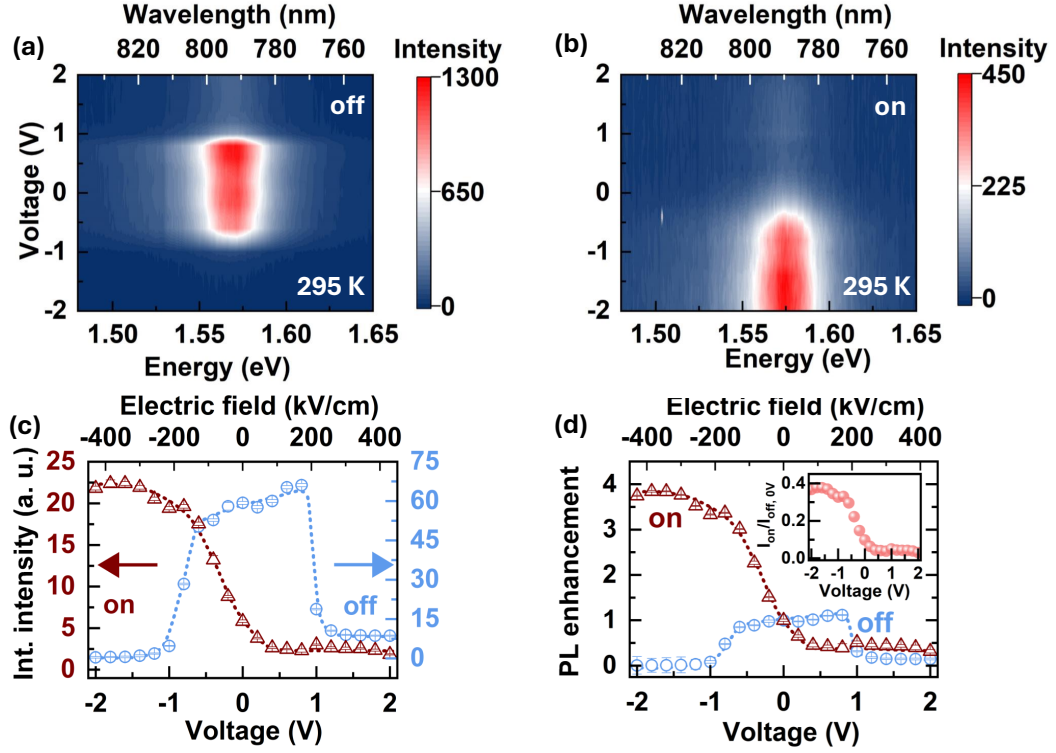


FIG. 3. (a) and (b) Contour plots of PL spectra as a function of voltage at the ‘off’ and ‘on’ positions, respectively. (c) Extracted energy integrated PL intensity, as described in Fig. 2a and b, with blue circles representing the ‘off’ position and red triangles representing the ‘on’ position. (d) Enhancement of the integrated intensity relative to its value at $V = 0$ V. Inset: revival of the intensity at the ‘on’ position compared to the ‘off’ position at $V = 0$ V.

contrast, applying a negative voltage ($V < 0$) reverses the field direction. Contour color plots of the PL spectra for the ‘off’ and ‘on’ positions are presented in Fig. 3a and b, respectively. The integrated intensities at both positions are displayed in Fig. 3c, with blue circles and red triangles representing the ‘off’ and ‘on’ positions, respectively. The integrated intensity exhibits a step-like variation: the ‘off’ position shows a two-step change, while the ‘on’ position demonstrates a single-step behavior. For the ‘off’ position, the PL intensity increases slightly at $V \sim +0.8$ V, reaching a maximum before rapidly decreasing at higher voltages. Similarly, a sharp decrease is observed below $V \sim -0.6$ V. For the ‘on’ position, a notable enhancement in PL intensity occurs at $V \sim -1.8$ V. The PL enhancement factor, defined as I_V/I_0 , where I_V is the PL intensity integrated over energy at a given voltage and I_0 is the integrated intensity at zero voltage, is illustrated in Fig. 3d. A modest increase of a factor of $\sim 1.1\times$ is observed for the ‘off’ position, while the ‘on’ position shows a maximum of $\sim 4.0\times$ enhancement. However, at a fixed position, the absolute change in intensity over the applied voltage sweep is much more pronounced, with nearly three orders of magnitude for the ‘off’ position and one order of magnitude for the ‘on’ position, respectively.

In a previous study, a thin hBN layer was used to achieve resonant tunneling of energetic electrons from graphene to MoSe₂ [35]. However, the structural differences in the present work, particularly the use of a thicker hBN layer, rule out this mechanism as the source of the observed PL enhancement. Moreover, the enhancement achieved at different polarities differs between the two positions: $V > 0$ for the bare-MoSe₂ and $V < 0$ for the MoSe₂/NbSe₂ heterostructure. A direct comparison of the PL intensity between the ‘on’ and ‘off’ positions at $V=0$, is shown as an intensity ratio in the inset of Fig. 3d. This reveals that the electrostatic field revives the optical intensity of the heterostructure to $\sim 40\%$ of the bare-MoSe₂ PL intensity, as shown in the inset of Fig. 3d. The maximum enhancement

factor, although, is different for another similarly structured device (D2) studied, achieving up to $12\times$ enhancement, $\sim 80\%$ of the bare-MoSe₂ intensity, as illustrated in Fig. S3. Interlayer coupling between MoSe₂ and NbSe₂, as well as the overall sample quality, plays a crucial role in this behavior.

Notably, different polarities of V are required to achieve enhancement at the two positions. To further substantiate this finding, we replaced NbSe₂ with a few-layer graphene atop MoSe₂ in third device D3. In this configuration, PL enhancement was observed for both bare-MoSe₂ and graphene/MoSe₂ heterostructure at $V > 0$, as shown in Fig. S4. The maximum enhancement factors are $\sim 1.2\times$ for bare-MoSe₂ and $\sim 3.8\times$ for graphene/MoSe₂ heterostructure, respectively. The result suggests a PL recovery of $\sim 23\%$ for ‘on-graphene’ heterostructure position compared to the bare-MoSe₂. Therefore, regardless of the metal used, the observed enhancement and its polarity-dependent behavior are governed by the metal’s position relative to ML-TMDCs and the direction of the applied voltage, respectively.

Temperature dependence

The exciton lifetime of bare-MoSe₂ is a few-nanoseconds at $T = 295$ K and a few-picoseconds at low temperatures ($T = 20$ K), as presented in Fig. S5a and b, respectively, and also reported earlier [9, 36]. This results in significant changes in exciton luminescence with varying temperature. To investigate the impact of radiative lifetime of exciton on PL quenching and their modification under an applied electric field in MoSe₂/NbSe₂ heterostructure under different thermal conditions, we conducted voltage-dependent studies at various temperatures. For comparison, contour plots for both the positions at $T = 20$ K are presented in Fig. 4a and b. Both the plots reveal two prominent peaks corresponding to excitons at ~ 1.65 eV and trions at ~ 1.62 eV. Although the mass action law predicts a constant trion-to-exciton intensity ratio in the absence of intentional doping, we observe a strong voltage dependence, likely due to photo-induced doping effects [37–40]. To maintain consistency with the present study’s theme, we focus on the exciton behavior. In contrast to $T = 295$ K, the PL-enhancement factor of the exciton for the ‘on’ position reduces at $T = 20$ K, while maintaining a qualitatively similar voltage-dependence. The maximum enhancements at specific temperatures for both positions are shown in Fig. 4c, with circles and triangles representing ‘off’ and ‘on’ positions, respectively. Fig. 4d demonstrates that the maximum enhancement factor depends on temperature. Notably, the maximum enhancement factor at the ‘off’ position remains ($\sim 1.1 \pm 0.1$), independent of temperature. In contrast, the maximum enhancement factor for the ‘on’ position decreases continuously from ~ 4.0 to 1.2 as the temperature is lowered from 295 K to 20 K.

III. DISCUSSION

To explain the field dependence of PL at the ‘off’ and ‘on’ positions we carried out a detailed analysis of $\Delta R/R$ spectra at these two points as shown in Fig. 5a and b, respectively, at $T = 295$ K. A clear vertical electric field dependence in $\Delta R/R$ spectra at ‘off’ position can be seen. For a more quantitative understanding, we have fitted each experimental spectrum using the Faddeeva function [41] (see Fig. S6) to extract the exciton peak position and oscillator strength (f). For ML TMDC, due to the lack of inversion symmetry and the absence of a net exciton dipole moment ($\Delta\mu = 0$), the field dependence of excitons exhibits a quadratic behavior, as shown in Fig. S7. This yields an exciton polarizability (α) of $(1.3 \pm 0.07) \times 10^{-18}$ eV·(m/V)². The estimated α is consistent with previously reported values [42], however, lower than the theoretically calculated value of 2×10^{-20} eV·(m/V)² [43]. The variation of the normalized oscillator strength ($\Delta f = \frac{fV - f_0}{f_0}$) for bare-MoSe₂, extracted from the fitting, is shown in Fig. 5c, where f_0 corresponds to zero applied voltage. Based on the α value from Fig. S7, the variation of absorption (A) is calculated

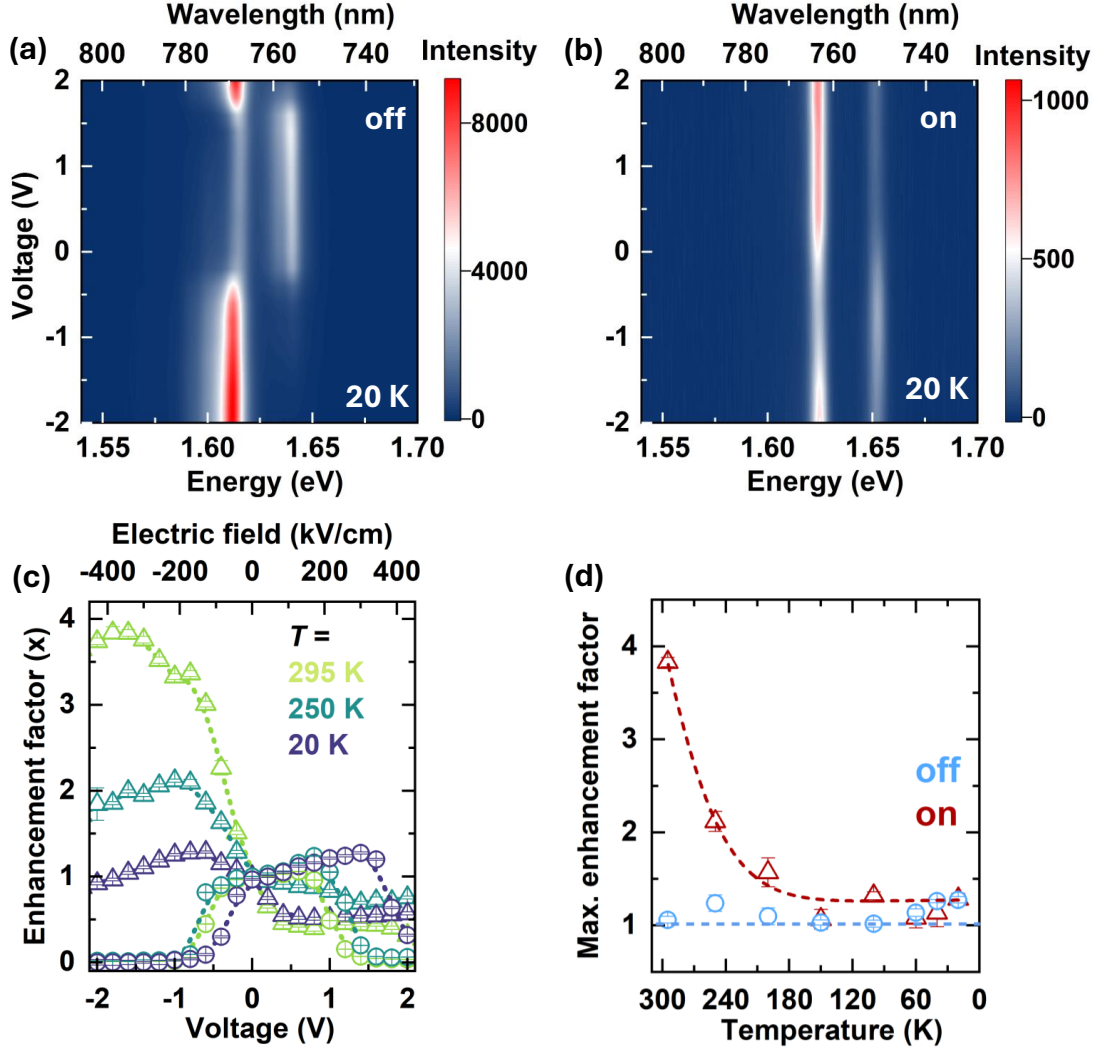


FIG. 4. Variation of PL emission with voltage at $T = 20$ K for (a) ‘off’ and (b) ‘on’ position. (c) Enhancement for ‘off’ position (circle) and ‘on’ position (triangle) at selective temperatures. (d) Observed maximum enhancement at each temperature at these points. Dashed lines are a guide to the eye.

with respect to electric field F . This calculation follows [44]

$$\Delta A(F) \propto \frac{dA}{dE} \left[-\Delta \vec{\mu} \cdot \vec{F} - \frac{1}{2} \alpha F^2 \right] \quad (1)$$

For bare-MoSe₂, $\frac{dA}{dE}$ at 1.57 eV is assumed to be proportional to $\frac{d(\Delta R)}{dE}$ at the same energy. The resulting ΔA , calculated using Eq. 1 with $\Delta \mu = 0$, is shown by the solid line in Fig. 5c. It closely matches the experimental data and highlights key trends. Therefore, this change in the oscillator strength explains the variation of PL at the ‘off’ position. A slight positive voltage is required to achieve the maximum PL intensity by countering the intrinsic n -type doping caused by selenium (Se) vacancies in MoSe₂.

To further corroborate the experimental observation at the ‘off’ position, we performed a model calculation using the transfer matrix method. The differential reflectance was obtained by considering a stack comprising the following sequence of layers: Air/few-layer-graphene/hBN/MoSe₂/hBN/few-layer-graphene/SiO₂/Si. The resulting $\Delta R/R$ val-

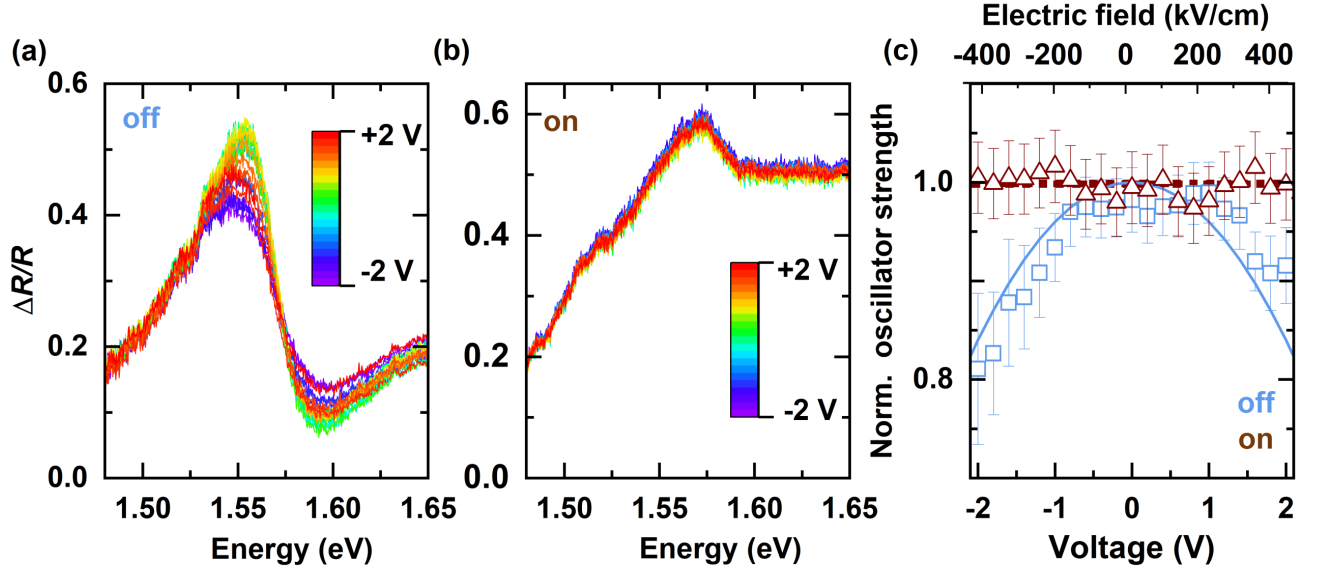


FIG. 5. (a) and (b) Reflectance contrast ($\Delta R/R$) plots at the ‘off’ and ‘on’ position with voltage at $T = 295$ K. (c) Variation in normalized oscillator strength at these positions.

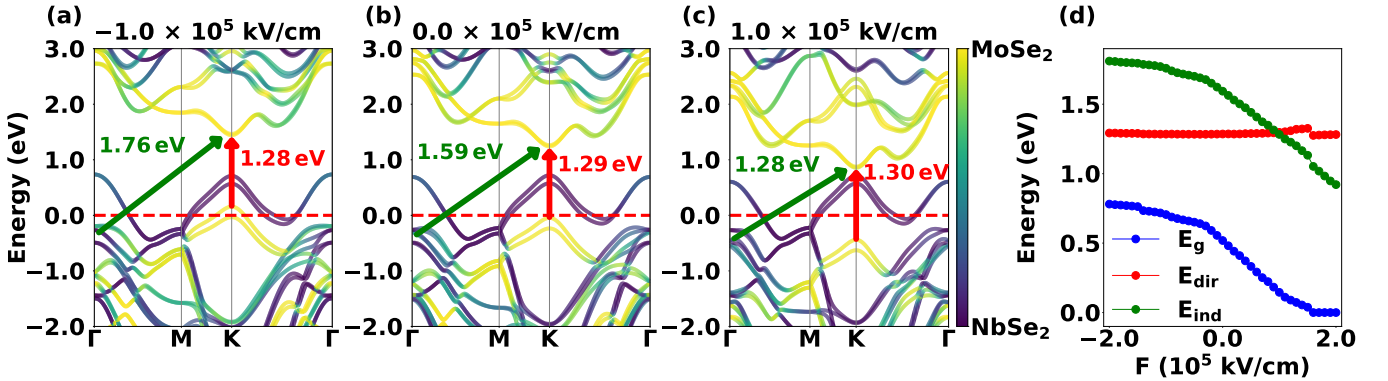


FIG. 6. Calculated bandstructure of $\text{MoSe}_2/\text{NbSe}_2$ heterostructure under vertical electric fields and the corresponding band gaps: (a) $F = -1.0 \times 10^5$ kV/cm, $E_g = 0.71$ eV, (b) $F = 0.0 \times 10^5$ kV/cm, $E_g = 0.52$ eV and (c) $F = +1.0 \times 10^5$ kV/cm, $E_g = 0.15$ eV. (d) The estimated band gap energy as an approximate measure of the optical transition energy as a function of the applied electric field.

ues, shown in Fig. S8b, exhibit a variation similar to that observed in the experiment in Fig. 3c, thereby validating the optical modeling. In addition, a perturbative analysis is employed to quantify the influence of the electric field on exciton properties. In particular, the exciton oscillator strength is approximately proportional to the square of the electron-hole e - h overlap. The electric field pulls electrons and holes in opposite directions, thereby reducing their overlap. The calculation reveals that the e - h overlap decreases with increasing field strength by a factor of $\frac{1}{1+(F/F_0)^2}$, where the characteristic field is $F_0 = 2450$ kV/cm, as shown in Fig. S8c. This reduction in e - h overlap directly contributes to a suppression of exciton recombination, and hence, the modulation of PL intensity observed at the ‘off’ position in Fig. 4c.

Fig. 5c shows that, unlike the ‘off’ position, the $\Delta R/R$ signal at the ‘on’ position exhibits negligible variation with V , indicating that changes in PL intensity are not due to absorption variations as seen in bare-MoSe₂. Therefore, to uncover the origin of the PL behavior at the ‘on’ position, we performed density functional theory (DFT) calculations, investigating the electronic band structures and analyzing their impact on the intensity of bandgap transitions. An intense optical transition requires a direct band gap with significant contributions from MoSe₂ states in both valence and conduction bands. Conversely, an indirect band gap is associated with weak band-gap emission. Hence, to address this question, bands in the vicinity of the band gap must be projected onto the parent MoSe₂ and NbSe₂ layers to ascertain the direct/indirect nature of the transition.

Our DFT-based calculations of MoSe₂/NbSe₂ heterostructures (assuming a single ML of each material) include spin-orbit coupling (SOC) and employ a localized basis set, enabling accurate treatment of strong perpendicular electric fields (see Methods). Specifically, standard plane-wave bases with supercells extended perpendicular to the layers are avoided, as they produce spurious field-induced states at the supercell boundaries. We assume AB stacking corresponding to a single MoSe₂/NbSe₂ structural unit in the unit cell. This necessarily implies that individual layers are strained relative to their free-standing structures. Importantly, such commensurate geometries mean that MoSe₂ and NbSe₂ layers are strongly coupled electronically. Effectively, metal- and semiconductor-derived states become interlocked and, thereby, less susceptible to electric fields. Conversely, decoupled layers are highly susceptible to electric fields since the dipole moment $F \times d$, where d is the center-to-center distance between the Se atoms of the two layers, will cause significant vertical shifts in the band structure.

The calculated band structures are shown in Fig. 6a-c. In particular, the band structure in the absence of an electric field verifies that MoSe₂/NbSe₂ has a direct band gap between semiconductor-derived bands (Fig. 6b). However, in the presence of electric fields, the indirect band gap shrinks in proportion to the field in the positive direction, while negative fields enlarge the indirect gap, c.f. Fig. 6a and Fig. 6c. This is in agreement with experimental spectra in Fig. 3d. However, the field required for indirect and direct band gaps to cross is $\sim 1.0 \times 10^5$ kV/cm, as shown in Fig. 6d, far greater than the experimentally observed range. We suggest that the discrepancy arises from the fact that the experimental MoSe₂/NbSe₂ heterojunctions are not commensurate but, rather, rotated relative to each other. Thereby, the electronic coupling is significantly weakened, leading to a reduction of the field required for a transition to an indirect band gap. Furthermore, the temperature variation in the maximum PL enhancement factor at the ‘on’ position can be attributed to radiative recombination competing with ultrafast charge and energy transfer processes in the TMDC/metal heterostructure. At low temperatures, the reduced exciton lifetime down to a few picoseconds means that radiative recombination dominates. In contrast, at $T = 295$ K, non-radiative channels contribute significantly, leading to a decreased PL enhancement.

IV. CONCLUSION

In summary, our findings reveal a significant enhancement of emission in TMDC/metal vdW heterostructures, enabled by electric field control. By applying a vertical electric field, we demonstrate the ability to tune the absolute PL intensity—by up to three orders of magnitude at the ‘off’ position and one order at the ‘on’ position. Such large modulation is promising for applications in electrically controlled switches and modulators, as suggested by previous studies [45, 46]. The variation at the ‘off’ position is linked to the modification of the excitonic oscillator strength, while calculated band structures demonstrate field-dependent modifications of the bandgap at the ‘on’ position. Temperature-dependent measurements reveal the impact of radiative recombination in PL enhancement

factor. This work underscores the potential of utilizing vertical electric fields as a precise and effective method to tailor excitonic and electronic properties in TMDC-based heterostructures. Unlike conventional tuning methods based on chemical doping or strain, our electric-field approach offers clean, reversible, and disorder-free control of exciton behavior. Moreover, our findings act as a guiding light for further exploration of 2D superconductors based TMDCs heterostructures below the superconducting critical transition temperatures. This can open interesting avenues to investigate the emergent quantum states influencing superconducting pairing mechanism and the excitonic physics.

METHODS

Device fabrication: The devices were fabricated via mechanical exfoliation of bulk crystals, followed by dry transfer using a polyDimethylSiloxane (PDMS) film onto the prepatterned electrodes. Details of the electron beam lithography (EBL) process for electrode patterning are provided in the Supplementary section. Monolayer MoSe₂ was obtained by exfoliation of a bulk crystal grown via chemical vapor deposition, while all other bulk crystals were purchased from HQ Graphene. The thickness of the hBN flakes was measured by an atomic force microscope.

Optical spectroscopy: Photoluminescence (PL) measurements were carried out using a continuous-wave 532 nm laser, focused to a $\sim 1 \mu\text{m}$ spot with a Mitutoyo objective ($\times 50$, 0.65 NA). The incident pump power was controlled using adjustable optical density filters in the excitation path. For reflection measurements, a white light laser (SuperK Extreme, NKT Photonics) was used.

Computational details: Density-functional calculations were performed using the GPAW software package [47]. A localized dzp-zeta basis combined with a $15 \times 15 \times 1$ k-space grid was employed, and all results are based on the PBE exchange-correlation functional including d3 van der Waals corrections. Spin-orbit interactions are included, and the AB-stacking unit cell was relaxed, yielding residual forces below $0.05 \text{ eV}/\text{\AA}$. The application of an electric field has a minor but significant effect on the atomic positions in the unit cell. Therefore, the structure was relaxed for all applied electric fields. The indirect bandgap is defined as the difference between the K-point energy of the first conduction band, where MoSe₂ contributes most strongly, and the average Γ -point energy of the six bands immediately below the Fermi level. There are a total of six bands due to spin-orbit coupling (SOC)-induced splittings, but the resulting SOC-induced splittings at the Γ -point are negligible. We use their average energy since all six bands exhibit some degree of hybridization, and the extent of this hybridization varies with the applied field strength.

DATA AVAILABILITY

The data that support the findings of this study are available from the corresponding author upon reasonable request.

ACKNOWLEDGMENTS

We gratefully acknowledge funding by the Deutsche Forschungsgemeinschaft (DFG, German Research Foundation) within the projects Ho5194/16-1 and INST 93/1025-1 FUGG. S.H and A.P. acknowledge the funding from the lighthouse project IQ-Sense of the Bavarian State Ministry of Science and the Arts as part of the Bavarian Quantum Initiative Munich Quantum Valley (15 02 TG 86). S.H., S.K. and C.G.M acknowledge financial support from the Würzburg-Dresden Cluster of Excellence on Complexity and Topology in Quantum Matter ct.qmat (EXC 2147, DFG

project ID 390858490). T.G.P. was supported by the DNRF Centre CLASSIQUE sponsored by the Danish National Research Foundation, grant nr. 187. S.A.T acknowledges primary support from DOE-SC0020653 (excitonic tests on crystals). Partial support comes from NSF CBET 2330110 (environmental stability tests). S.A.T. also acknowledges partial support from Applied Materials Inc. and Lawrence Semiconductor Labs for growth systems. We are grateful for enabling us to have used the Raman measurement facility at the Julius-Maximilians-Universität Würzburg, Experimental Physics 6.

CONFLICT OF INTEREST

The authors declare no competing interests.

-
- [1] Q. Tong, H. Yu, Q. Zhu, Y. Wang, X. Xu, and W. Yao, Topological mosaics in moiré superlattices of van der Waals heterobilayers, *Nat. Phys.* **13**, 356 (2017).
 - [2] T. Li, S. Jiang, L. Li, Y. Zhang, K. Kang, J. Zhu, K. Watanabe, T. Taniguchi, D. Chowdhury, L. Fu, *et al.*, Continuous mott transition in semiconductor moiré superlattices, *Nature* **597**, 350 (2021).
 - [3] R. Xiong, J. H. Nie, S. L. Brantly, P. Hays, R. Sailus, K. Watanabe, T. Taniguchi, S. Tongay, and C. Jin, Correlated insulator of excitons in WSe₂/WS₂ moiré superlattices, *Science* **380**, 860 (2023).
 - [4] L. Ma, P. X. Nguyen, Z. Wang, Y. Zeng, K. Watanabe, T. Taniguchi, A. H. MacDonald, K. F. Mak, and J. Shan, Strongly correlated excitonic insulator in atomic double layers, *Nature* **598**, 585 (2021).
 - [5] G. Xu, X. Zhou, W. Chen, G. Hu, Z. Yan, Z. Li, S. Yang, and C.-W. Qiu, Hydrodynamic moiré superlattice, *Science* **386**, 1377 (2024).
 - [6] Y. Meng, T. Wang, C. Jin, Z. Li, S. Miao, Z. Lian, T. Taniguchi, K. Watanabe, F. Song, and S.-F. Shi, Electrical switching between exciton dissociation to exciton funneling in MoSe₂/WS₂ heterostructure, *Nat. Commun.* **11**, 2640 (2020).
 - [7] N. Ubrig, E. Ponomarev, J. Zultak, D. Domaretskiy, V. Zólyomi, D. Terry, J. Howarth, I. Gutiérrez-Lezama, A. Zhukov, Z. R. Kudrynskiy, *et al.*, Design of van der Waals interfaces for broad-spectrum optoelectronics, *Nat. Mater.* **19**, 299 (2020).
 - [8] P. Rivera, J. R. Schaibley, A. M. Jones, J. S. Ross, S. Wu, G. Aivazian, P. Klement, K. Seyler, G. Clark, N. J. Ghimire, *et al.*, Observation of long-lived interlayer excitons in monolayer MoSe₂–WSe₂ heterostructures, *Nat. Commun.* **6**, 6242 (2015).
 - [9] C. Robert, D. Lagarde, F. Cadiz, G. Wang, B. Lassagne, T. Amand, A. Balocchi, P. Renucci, S. Tongay, B. Urbaszek, *et al.*, Exciton radiative lifetime in transition metal dichalcogenide monolayers, *Phys. Rev. B* **93**, 205423 (2016).
 - [10] M. Palummo, M. Bernardi, and J. C. Grossman, Exciton radiative lifetimes in two-dimensional transition metal dichalcogenides, *Nano Lett.* **15**, 2794 (2015).
 - [11] Y. Liu, H. Fang, A. Rasmita, Y. Zhou, J. Li, T. Yu, Q. Xiong, N. Zheludev, J. Liu, and W. Gao, Room temperature nanocavity laser with interlayer excitons in 2D heterostructures, *Sci. Adv.* **5**, eaav4506 (2019).
 - [12] J. F. Gonzalez Marin, D. Unuchek, Z. Sun, C. Y. Cheon, F. Tagarelli, K. Watanabe, T. Taniguchi, and A. Kis, Room-temperature electrical control of polarization and emission angle in a cavity-integrated 2D pulsed LED, *Nat. Commun.* **13**, 4884 (2022).
 - [13] Y. Meng, J. Feng, S. Han, Z. Xu, W. Mao, T. Zhang, J. S. Kim, I. Roh, Y. Zhao, D.-H. Kim, *et al.*, Photonic van der Waals integration from 2D materials to 3D nanomembranes, *Nat. Rev. Mater.* **8**, 498 (2023).
 - [14] B. Yang, E. Molina, J. Kim, D. Barroso, M. Lohmann, Y. Liu, Y. Xu, R. Wu, L. Bartels, K. Watanabe, *et al.*, Effect of distance on photoluminescence quenching and proximity-induced spin–orbit coupling in graphene/WSe₂ heterostructures, *Nano Lett.* **18**, 3580 (2018).

- [15] E. Lorchat, L. E. P. López, C. Robert, D. Lagarde, G. Froehlicher, T. Taniguchi, K. Watanabe, X. Marie, and S. Berciaud, Filtering the photoluminescence spectra of atomically thin semiconductors with graphene, *Nat. Nanotechnol.* **15**, 283 (2020).
- [16] Y. Liu, P. Stradins, and S.-H. Wei, Van der Waals metal-semiconductor junction: Weak fermi level pinning enables effective tuning of schottky barrier, *Sci. Adv.* **2**, e1600069 (2016).
- [17] X. Xi, L. Zhao, Z. Wang, H. Berger, L. Forró, J. Shan, and K. F. Mak, Strongly enhanced charge-density-wave order in monolayer NbSe₂, *Nat. Nanotechnol.* **10**, 765 (2015).
- [18] J. Joshi, T. Zhou, S. Krylyuk, A. V. Davydov, I. Zutic, and P. M. Vora, Localized excitons in NbSe₂-MoSe₂ heterostructures, *ACS nano* **14**, 8528 (2020).
- [19] C. Li, Z. Wu, C. Zhang, S. Peng, J. Han, M. He, X. Dong, J. Gou, J. Wang, and Y. Jiang, Self-powered photodetector with high performance based on all-2D NbSe₂/MoSe₂ van der Waals heterostructure, *Adv. Opt. Mater.* **11**, 2300905 (2023).
- [20] K. F. Mak and J. Shan, Photonics and optoelectronics of 2D semiconductor transition metal dichalcogenides, *Nat. Photonics* **10**, 216 (2016).
- [21] T. Chu, H. Ilatikhameneh, G. Klimeck, R. Rahman, and Z. Chen, Electrically tunable bandgaps in bilayer MoS₂, *Nano Lett.* **15**, 8000 (2015).
- [22] A. Ramasubramaniam, D. Naveh, and E. Towe, Tunable band gaps in bilayer transition-metal dichalcogenides, *Phys. Rev. B* **84**, 205325 (2011).
- [23] M. Kang, B. Kim, S. H. Ryu, S. W. Jung, J. Kim, L. Moreschini, C. Jozwiak, E. Rotenberg, A. Bostwick, and K. S. Kim, Universal mechanism of band-gap engineering in transition-metal dichalcogenides, *Nano Lett.* **17**, 1610 (2017).
- [24] A. M. Jones, H. Yu, N. J. Ghimire, S. Wu, G. Aivazian, J. S. Ross, B. Zhao, J. Yan, D. G. Mandrus, D. Xiao, *et al.*, Optical generation of excitonic valley coherence in monolayer WSe₂, *Nat. Nanotechnol.* **8**, 634 (2013).
- [25] S. Wu, J. S. Ross, G.-B. Liu, G. Aivazian, A. Jones, Z. Fei, W. Zhu, D. Xiao, W. Yao, D. Cobden, *et al.*, Electrical tuning of valley magnetic moment through symmetry control in bilayer MoS₂, *Nat. Phys.* **9**, 149 (2013).
- [26] L. A. Jauregui, A. Y. Joe, K. Pistunova, D. S. Wild, A. A. High, Y. Zhou, G. Scuri, K. De Greve, A. Sushko, C.-H. Yu, *et al.*, Electrical control of interlayer exciton dynamics in atomically thin heterostructures, *Science* **366**, 870 (2019).
- [27] J. Kistner-Morris, A. Shi, E. Liu, T. Arp, F. Farahmand, T. Taniguchi, K. Watanabe, V. Aji, C. H. Lui, and N. Gabor, Electric-field tunable Type-I to Type-II band alignment transition in MoSe₂/WS₂ heterobilayers, *Nat. Commun.* **15**, 4075 (2024).
- [28] D. Li, R. Cheng, H. Zhou, C. Wang, A. Yin, Y. Chen, N. O. Weiss, Y. Huang, and X. Duan, Electric-field-induced strong enhancement of electroluminescence in multilayer molybdenum disulfide, *Nat. Commun.* **6**, 7509 (2015).
- [29] N. Leisgang, S. Shree, I. Paradisanos, L. Sponfeldner, C. Robert, D. Lagarde, A. Balocchi, K. Watanabe, T. Taniguchi, X. Marie, *et al.*, Giant stark splitting of an exciton in bilayer MoS₂, *Nat. Nanotechnol.* **15**, 901 (2020).
- [30] E. Lorchat, M. Selig, F. Katsch, K. Yumigeta, S. Tongay, A. Knorr, C. Schneider, and S. Höfling, Excitons in bilayer MoS₂ displaying a colossal electric field splitting and tunable magnetic response, *Phys. Rev. Lett.* **126**, 037401 (2021).
- [31] Q. Shi, E.-M. Shih, D. Rhodes, B. Kim, K. Barmak, K. Watanabe, T. Taniguchi, Z. Papić, D. A. Abanin, J. Hone, *et al.*, Bilayer WSe₂ as a natural platform for interlayer exciton condensates in the strong coupling limit, *Nat. Nanotechnol.* **17**, 577 (2022).
- [32] X. Lv, W. Wei, P. Zhao, J. Li, B. Huang, and Y. Dai, Tunable schottky contacts in MSe₂/NbSe₂ (M= Mo and W) heterostructures and promising application potential in field-effect transistors, *Phys. Chem. Chem. Phys.* **20**, 1897 (2018).
- [33] Y. Li, A. Chernikov, X. Zhang, A. Rigosi, H. M. Hill, A. M. Van Der Zande, D. A. Chenet, E.-M. Shih, J. Hone, and T. F. Heinz, Measurement of the optical dielectric function of monolayer transition-metal dichalcogenides: MoS₂, MoSe₂, WS₂, and WSe₂, *Phys. Rev. B* **90**, 205422 (2014).
- [34] G. Froehlicher, E. Lorchat, and S. Berciaud, Charge versus energy transfer in atomically thin graphene-transition metal dichalcogenide van der Waals heterostructures, *Phys. Rev. X* **8**, 011007 (2018).
- [35] L. Wang, S. Papadopoulos, F. Iyikanat, J. Zhang, J. Huang, T. Taniguchi, K. Watanabe, M. Calame, M. L. Perrin, F. J. García de Abajo, *et al.*, Exciton-assisted electron tunnelling in van der Waals heterostructures, *Nat. Mater.* **22**, 1094

(2023).

- [36] H. Fang, B. Han, C. Robert, M. Semina, D. Lagarde, E. Courtade, T. Taniguchi, K. Watanabe, T. Amand, B. Urbaszek, *et al.*, Control of the exciton radiative lifetime in van der Waals heterostructures, *Phys. Rev. Lett.* **123**, 067401 (2019).
- [37] I. Verzhbitskiy, D. Vella, K. Watanabe, T. Taniguchi, and G. Eda, Suppressed out-of-plane polarizability of free excitons in monolayer WSe₂, *ACS nano* **13**, 3218 (2019).
- [38] N. Zhang, A. Surrente, M. Baranowski, D. Dumcenco, Y.-C. Kung, D. K. Maude, A. Kis, and P. Plochocka, Impact of photodoping on inter-and intralayer exciton emission in a MoS₂/MoSe₂/MoS₂ heterostructure, *Appl. Phys. Lett.* **113** (2018).
- [39] J. G. Roch, N. Leisgang, G. Froehlicher, P. Makk, K. Watanabe, T. Taniguchi, C. Schonenberger, and R. J. Warburton, Quantum-confined stark effect in a MoS₂ monolayer van der Waals heterostructure, *Nano lett.* **18**, 1070 (2018).
- [40] N. Lundt, E. Cherotchenko, O. Iff, X. Fan, Y. Shen, P. Bigenwald, A. Kavokin, S. Höfling, and C. Schneider, The interplay between excitons and trions in a monolayer of MoSe₂, *Appl. Phys. Lett.* **112** (2018).
- [41] A. Raja, L. Waldecker, J. Zipfel, Y. Cho, S. Brem, J. D. Ziegler, M. Kulig, T. Taniguchi, K. Watanabe, E. Malic, *et al.*, Dielectric disorder in two-dimensional materials, *Nat. Nanotechnol.* **14**, 832 (2019).
- [42] A. Chernenko, A. Brichkin, and G. Golyshkov, Stark effect in a heterostructure based on a mose₂ monolayer, *Bull. Russ. Acad. Sci.: Phys.* **88**, 213 (2024).
- [43] T. G. Pedersen, Exciton stark shift and electroabsorption in monolayer transition-metal dichalcogenides, *Phys. Rev. B* **94**, 125424 (2016).
- [44] L. Sebastian, G. Weiser, and H. Bässler, Charge transfer transitions in solid tetracene and pentacene studied by electroabsorption, *Chem. Phys.* **61**, 125 (1981).
- [45] Z. Sun, A. Martinez, and F. Wang, Optical modulators with 2D layered materials, *Nat. Photonics* **10**, 227 (2016).
- [46] T.-Z. Shen, S.-H. Hong, and J.-K. Song, Electro-optical switching of graphene oxide liquid crystals with an extremely large kerr coefficient, *Nat. Mater.* **13**, 394 (2014).
- [47] J. Enkovaara, C. Rostgaard, J. J. Mortensen, J. Chen, M. Dulak, L. Ferrighi, J. Gavnholt, C. Glinsvad, V. Haikola, H. A. Hansen, *et al.*, Electronic structure calculations with GPAW: a real-space implementation of the projector-augmented-wave method, *J. Phys. Condens. Matter* **22**, 253202 (2010).

Supplementary Information for

Electrical Control of Excitons in Bare-MoSe₂ and MoSe₂/NbSe₂ Heterostructure

Atanu Patra,¹ Vishakha Kaushik,¹ Ali Sepas,² Subhamoy Sahoo,¹ Mathias Federolf,¹ Christian G. Mayer,^{1,3}
 Sebastian Klemmt,^{1,3} Monika Emmerling,¹ Simon Betzold,¹ Seth Ariel Tongay,⁴ Fabian Hartmann,¹ Thomas Garm
 Pedersen,² and Sven Höfling^{1,3}

¹*Julius-Maximilians-Universität Würzburg, Physikalisches Institut, Lehrstuhl für Technische Physik, Am Hubland,
 97074 Würzburg, Germany*

²*Department of Materials and Production, Aalborg University, DK-9220 Aalborg Øst, Denmark*

³*Physikalisches Institut and Würzburg-Dresden Cluster of Excellence ct.qmat, Germany*

⁴*Materials Science and Engineering, School for Engineering of Matter, Transport and Energy, Arizona State
 University, Tempe, 85287 Arizona, United States*

1. Supplementary Note-1

Pre-patterned gold-electrode

Electron beam lithography (EBL) is performed to define the small internal contacts with high precision. The process begins with spin-coating a 1 μm thick PMMA 950K resist layer, followed by a soft bake at 165°C for 2 minutes to ensure proper adhesion and solvent removal. EBL exposure is carried out using a 2 nA beam current at 100 kV acceleration voltage with a dose of 1000 $\mu\text{C}/\text{cm}^2$. After exposure, the resist is developed in MIBK/isopropanol(IPA) for 45 seconds, followed by a rinse in IPA to stop the development process. The patterned resist is then used for SiO_2 etching in the Sentech RIE SI 591 system, employing a reactive ion etching (RIE) process with CHF_3 (15 sccm) and Argon (7.5 sccm) at an RF power of 50 W for 300 seconds, achieving an etching depth of 50 nm. After etching, a thin metal layer is deposited, consisting of 3 nm chromium and 50 nm gold, followed by a lift-off process in methylpyrrolidone to define the contacts.

Next, an optical positive varnish layer of 2 μm ma-P1215 is applied, followed by optical exposure and development in MA-D331. To improve adhesion and remove organic residues, an O_2 plasma treatment for 2 minutes is performed. For the thick outer contacts, 30 nm chromium and 300 nm gold are deposited, followed by a lift-off process in methylpyrrolidone to complete the fabrication.

Thickness characterization

Figure S1a and b show the Raman spectra of bare- MoSe_2 and $\text{MoSe}_2/\text{NbSe}_2$ heterostructures, respectively. The y-axis is presented on a logarithmic scale to better resolve the peaks. In the spectrum of bare- MoSe_2 (Fig. S1a), a single peak is observed at $\sim 247 \text{ cm}^{-1}$, corresponding to the A_{1g} mode, which is the characteristic out-of-plane vibrational mode of ML MoSe_2 . In contrast, the spectrum of $\text{MoSe}_2/\text{NbSe}_2$ (Fig. S1b) exhibits two distinct additional peaks of NbSe_2 namely, the A_{1g} mode at $\sim 227 \text{ cm}^{-1}$ and the E_{1g} mode at 236 cm^{-1} . The separation between these two peaks ($\Delta \sim 9 \text{ cm}^{-1}$), together with the presence of a soft mode at $\sim 175 \text{ cm}^{-1}$, indicates that the NbSe_2 layer is of bulk thickness.

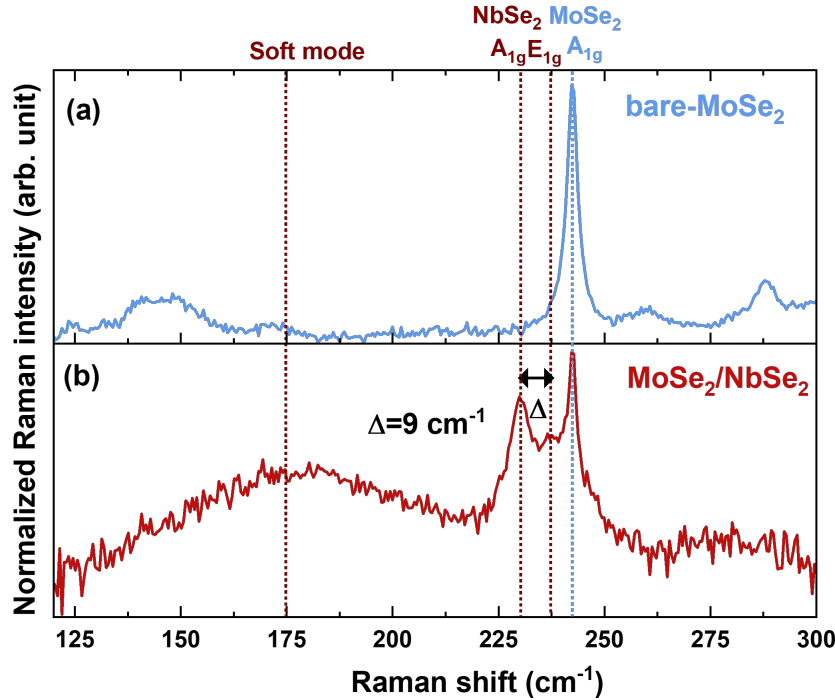


FIG. S1. Raman spectra of (a) bare- MoSe_2 and (b) $\text{MoSe}_2/\text{NbSe}_2$ heterostructure.

Linear regime of exciton

The linear increase of PL intensity in Fig. S2a, both bare-MoSe₂ and MoSe₂/NbSe₂ indicates that there is no loss due to exciton-exciton annihilation. In addition, Fig. S2b illustrates the PL quenching factor remains within the experimental error.

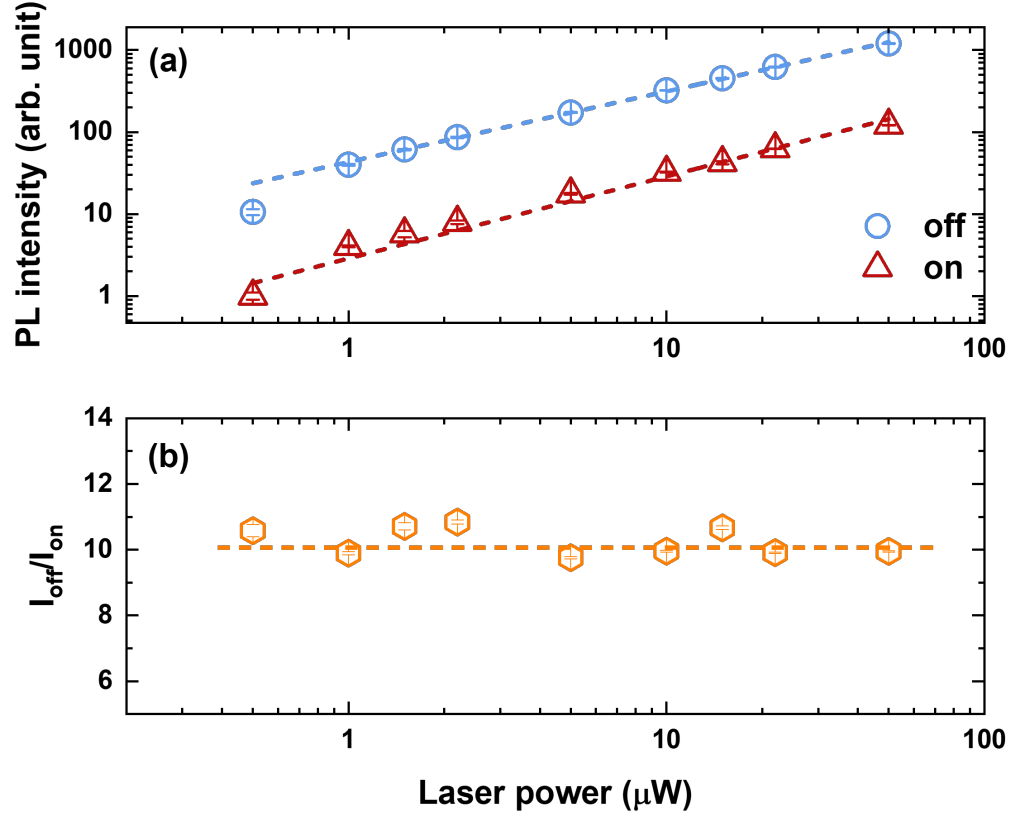


FIG. S2. (a) Power-dependent PL intensity at 'off' (blue) and 'on' (red) positions. (b) PL quenching at the 'on' position as a function of laser power, compared to 'off' position.

Voltage dependence of Device-2

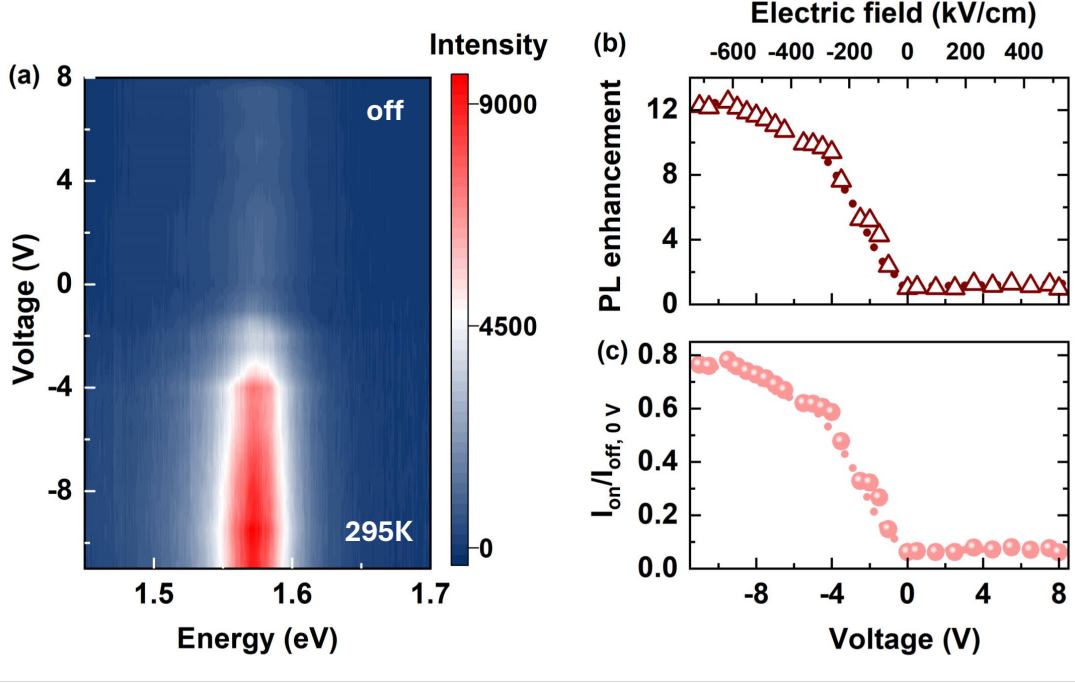


FIG. S3. Voltage dependence of Device-2. (a) Contour plot of PL spectra as a function of voltage at the ‘on’ position. (b) Enhancement of the integrated PL intensity relative to its value at $V = 0$ V. (c) Intensity variation relative to the PL intensity at the ‘off’ position at 0 V.

A voltage-dependent PL enhancement is observed in device D2 of the $\text{MoSe}_2/\text{NbSe}_2$ heterostructure, as shown in Fig. S3, similar to the behavior presented in the main text (Fig. 3b). Figure S3a shows the contour plot, and Fig. S3b displays the extracted integrated PL intensity as a function of voltage. The maximum enhancement factor reaches ~ 12 , and the PL revival is $\sim 80\%$ compared to bare- MoSe_2 , as shown in Fig. S3c.

Field calculation

The electric field is calculated in bare- MoSe_2 as²

$$F = \frac{V}{d_{Mo} + d_h \left(\frac{\epsilon_{\perp,0,Mo}}{\epsilon_{\perp,0,h}} \right)}$$

where $d_{Mo(h)}$ is the thickness of the ML- MoSe_2 (hBN), $\epsilon_{\perp,0,Mo}$ ($=7.2$) and $\epsilon_{\perp,0,h}$ ($=3.76$) are the static out-of-plane dielectric constants of MoSe_2 and hBN, respectively.

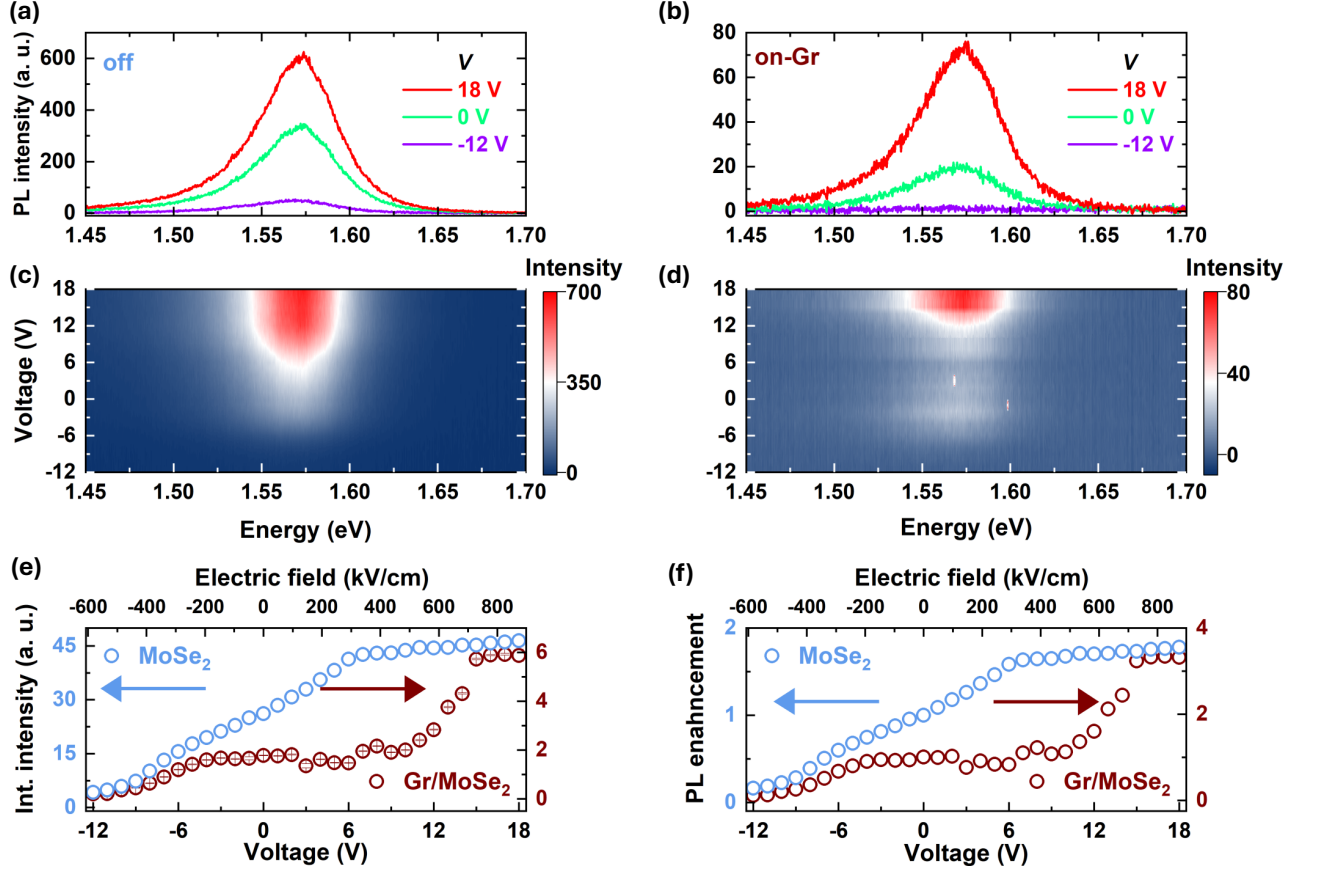


FIG. S4. Voltage dependence of PL in bare-MoSe₂ and FLG/MoSe₂ devices. (a) and (d) PL spectra at different gate voltages for the ‘off’ and ‘on-graphene’ positions. (b) and (e) Corresponding contour plots as a function of voltage. (c) Integrated PL intensity for ‘off’ (blue circles) and ‘on-graphene’ (red triangles) positions. (f) PL enhancement factor for the two positions.

Voltage dependence of Device-3

Another device (D3) with few-layer graphene (FLG) is placed on top of MoSe₂ as a metal contact instead of NbSe₂. Changing the position of the metal modifies the PL variation, as shown in Fig. S4. Representative PL spectra at different gate voltages for the ‘off’ and ‘on-graphene’ positions are shown in Fig. S4a and b, respectively. The corresponding contour plots as a function of voltage at the same positions are given in Fig. S4c and d. Importantly, in this case, PL enhancement occurs in the same direction for both positions. The integrated PL intensities are shown in Fig. S4e, with blue circles representing the ‘off’ position and red triangles representing the ‘on-graphene’ position. Fig. S4f indicates that the PL enhancement factors are $\sim 2\times$ and $3\times$ for the ‘off’ and ‘on-graphene’ positions, respectively.

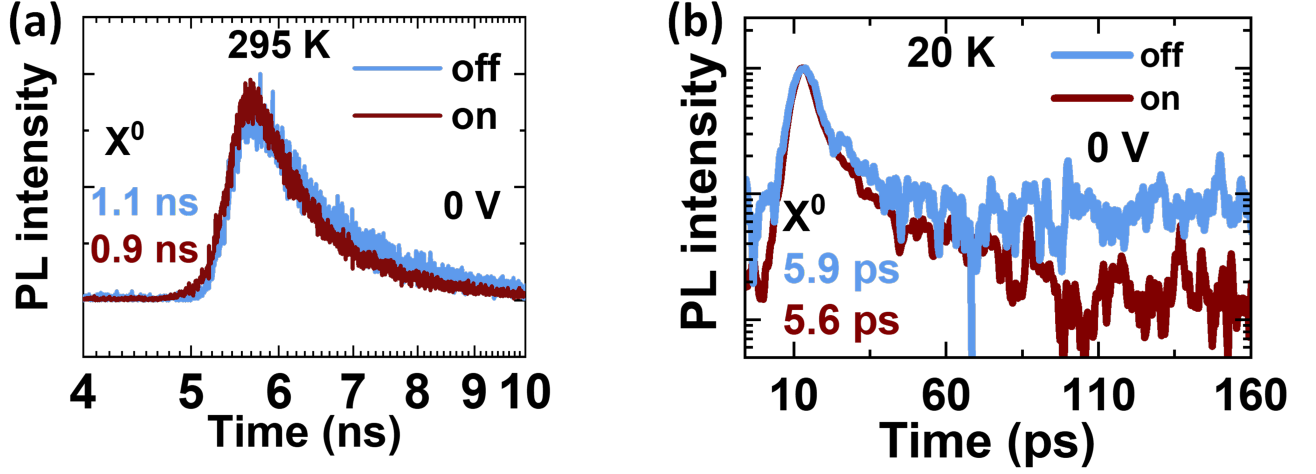


FIG. S5. Time-resolved PL measurements at room temperature ($T = 295$ K) (a) and at 20 K (b). Data at the ‘off’ and ‘on’ points are shown in blue and red, respectively.

Time-resolved measurements

To perform time-resolved measurements, a pulsed excitation laser is employed for precise probing of the emission lifetime. The excitation source is a Spectra-Physics Tsunami titanium-sapphire laser, which produces pulses with a duration of around 2 ps and operates at a repetition rate of 80 MHz. Since the lifetime of excitons undergoes significant changes when the sample is cooled to cryogenic temperatures, two distinct time-resolving techniques are implemented, each optimized for a different temporal range. To measure emission lifetimes within the nanosecond range, a PicoQuant τ -SPAD avalanche photodiode is utilized with a time-correlated single photon counting module, PicoHarp 300. For lifetimes down to just a few picoseconds, a Hamamatsu streak camera C10910 is used. The streak camera is equipped with a charge-coupled device (CCD) detector ORCA-Lightning, which enables simultaneous spectral and temporal resolution of the emission signal. In both the techniques, precise synchronization between the recorded signal and the pulsed excitation source is required. The synchronization for the PicoHarp 300 module is directly triggered by the electronic control system of the pulsed laser, whereas the streak camera uses an optical reference signal. This is achieved by placing an optical pick-up diode along the excitation beam path, which serves as a time reference for the streak camera. To ensure high spectral resolution, both time-resolving devices are positioned after an Andor Shamrock 750 Czerny–Turner monochromator. This monochromator spectrally disperses the emitted light along one axis before it is analyzed. Additionally, a Dove prism is incorporated into the setup to rotate the image before it is directed into either the streak camera or the avalanche photodiode, ensuring proper alignment of the spectral information in the detecting system. Time-resolved PL measurement at $T = 295$ K and $T = 20$ K in bare-MoSe₂ and MoSe₂/NbSe₂ are shown in blue and red, respectively.

Reflectance contrast analysis

To quantitatively analyze the exciton resonances, we fitted the reflectance contrast ($\Delta R/R$) using the Faddeeva function, as described in ref.³. Examples of the fitted spectra for bare-MoSe₂ and MoSe₂/NbSe₂ at $V = 0$ V are shown in Fig. S6a and b, respectively.

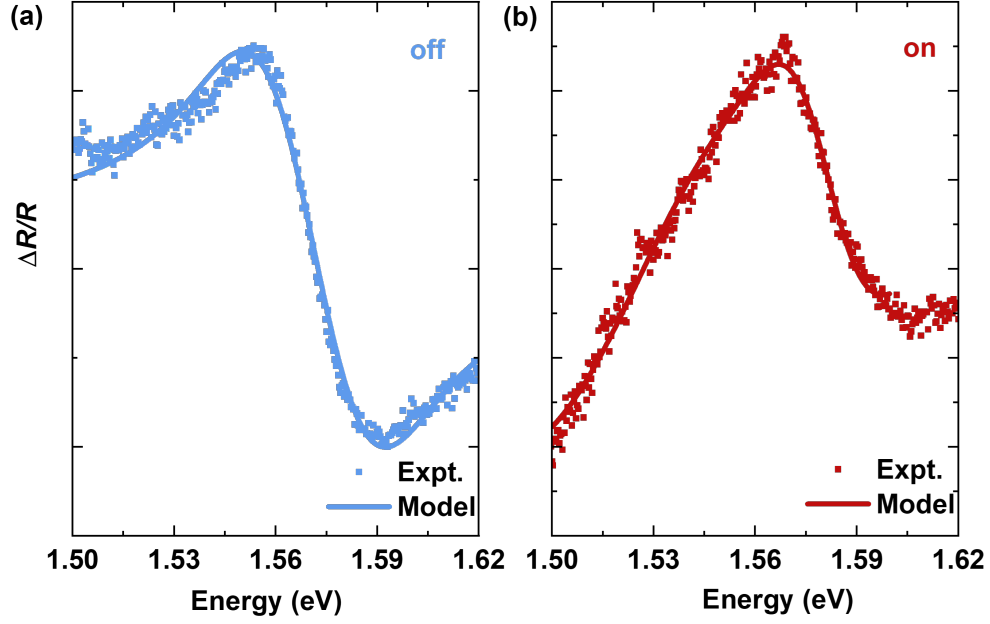


FIG. S6. Fitting of the reflectance contrast ($\Delta R/R$) of bare-MoSe₂ (a) and MoSe₂/NbSe₂ (b) using Faddeeva model as given in ref.³

Stark shift of monolayer MoSe₂

Variation of exciton peak position at room temperature against electric field (F) in bare-MoSe₂, as extracted from Fig. 5a in the main text. A quadratic dependence is evident in Fig. S7, corresponding to an exciton polarizability (α) of 1.50×10^{-18} eV·(m/V)².

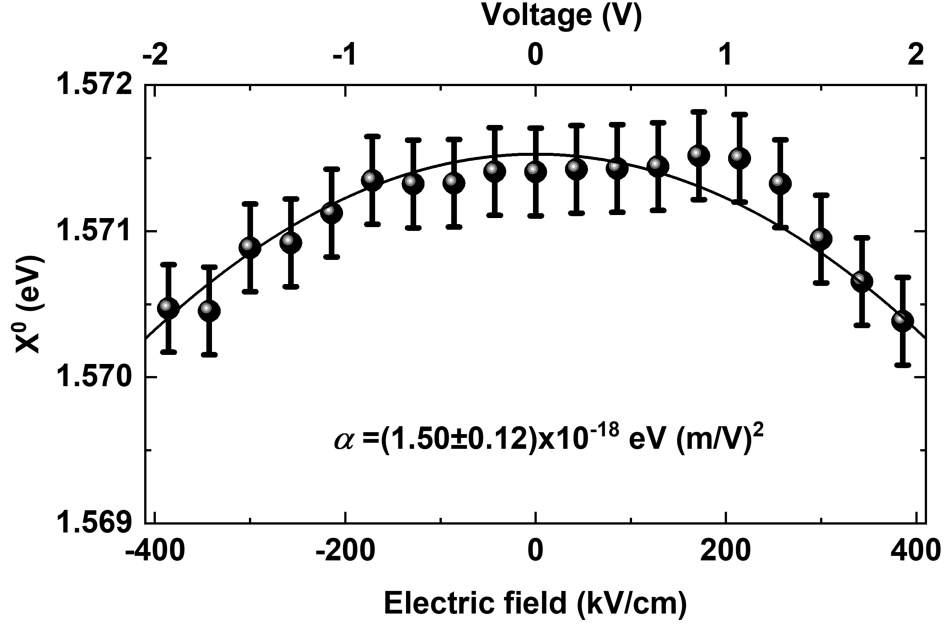


FIG. S7. Variation of A-exciton of bare-MoSe₂ with electric field.

Calculated reflectance contrast

The optical properties of the stack are modelled using the transfer matrix method. We calculate the differential reflectance by considering a stack comprising the following sequence of layers: Air/Gr/hBN/MoSe₂/hBN/Gr/SiO₂/Si, where Gr is designated as few-layer graphene. The stack is shown in Fig. S8a.

The parameters are taken as

$$\begin{aligned}
 d_{air} &= \infty, & n_{air} &= 1.0 \\
 d_{Si} &= \infty, & n_{Si} &= 3.7 \\
 d_{hBN} &= 12 \text{ nm}, & n_{hBN} &= 2.12 \\
 d_{Gr} &= 3.5 \text{ nm}, & n_{Gr} &= 3 + 2.5i \\
 d_{SiO_2} &= 100 \text{ nm}, & n_{SiO_2} &= 1.45
 \end{aligned}$$

The MoSe₂ is modelled following the approach in⁴ including excitonic and spin-orbit effects. Dielectric screening by encapsulation in hBN is incorporated using a dielectric constant of 4.5 in the Keldysh potential. In addition, a constant background contribution $\epsilon_{\infty} = 6$ is added to the excitonic response of MoSe₂.

The modification of the dielectric properties of MoSe₂ by a perpendicular external electric field is accounted for by including the reduced overlap between electrons and holes. Within the exciton envelope approximation, the exciton oscillator strength is determined by the electron-hole overlap. In an electric field, the carriers are pulled in opposite directions, leading to a reduced overlap. We model the effect by considering carriers in a 0.63 nm wide quantum well

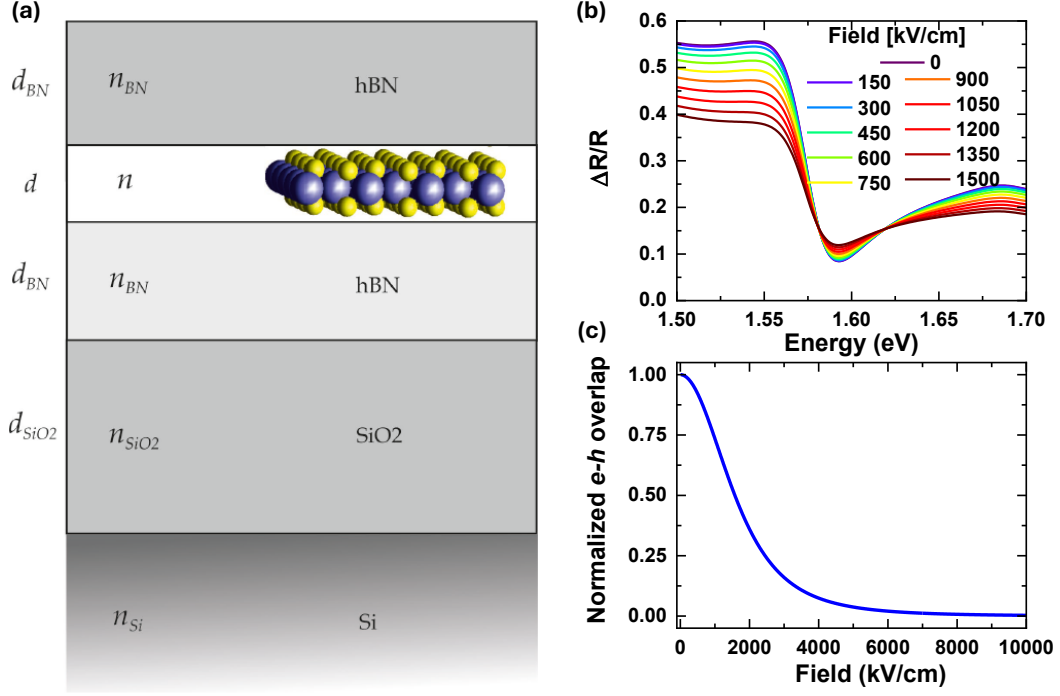


FIG. S8. (a) Sketch of the model. (b) Calculated variation of reflectance contrast ($\Delta R/R$) for different electric fields. (c) Calculated e - h overlap under vertical electric field (F).

with finite barriers of 0.5 eV. The effective masses are assumed identical and takes as twice the reduced mass for direct excitons in MoSe₂, see⁵. A perturbation calculation shows that oscillator strengths are reduced by a factor of $\frac{1}{\left(1 + \frac{F^2}{F_0^2}\right)^2}$, where the characteristic field is $F_0 = 2450$ kV/cm.

Leakage current

Another possibility of field dependence of PL intensity at the ‘on’ positions could be leakage current within the system. A $V > 0$, i.e. electrode near to MoSe₂ has a high potential, and the electrode close to NbSe₂ is at ground potential, induces a leakage current from top to bottom, corresponding to electron flow from NbSe₂ to MoSe₂. The work function of NbSe₂ lies below the valence band maximum (VBM) of MoSe₂. Hence, a positive current enhances the electron density in MoSe₂, converting neutral excitons to trions and reducing PL intensity. Additional free charge carriers increase Coulomb screening, lowering exciton binding energy and destabilizing excitons, leading to further PL quenching. Excess electrons may also enhance non-radiative pathways, such as Auger or defect-assisted recombination. Conversely, for $V < 0$, the current flow reverses direction, i.e., electrons flow from MoSe₂ to NbSe₂. Even for this condition, excitons are dissociating and therefore expected to exhibit PL reduction, contradicting the observed behavior. Furthermore, no significant leakage current is observed (see Fig. S9).

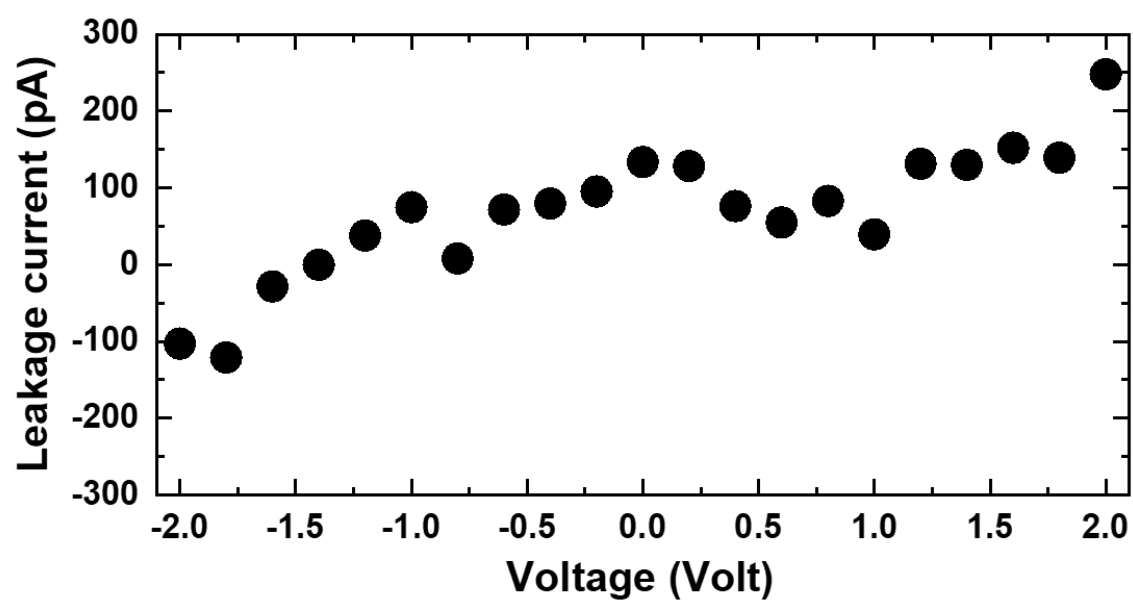


FIG. S9. Leakage current measured in Device-1.

REFERENCES

1. H. M. Hill, A. F. Rigosi, S. Krylyuk, J. Tian, N. V. Nguyen, A. V. Davydov, D. B. Newell, and A. R. Hight Walker; Comprehensive optical characterization of atomically thin NbSe₂, *Phys. Rev. B* **98**, 165109 (2018).
2. S. Das, M. Dandu, G. Gupta, K. Murali, N. Abraham, S. Kallatt, K. Watanabe, T. Taniguchi, K. Majumdar, Highly Tunable Layered Exciton in Bilayer WS₂: Linear Quantum Confined Stark Effect versus Electrostatic Doping, *ACS Photonics* **7**, 3386–3393 (2020).
3. A. Raja, L. Waldecker, J. Zipfel, Y. Cho, S. Brem, J. D. Ziegler, M. Kulig, T. Taniguchi, K. Watanabe, E. Malic, T. F. Heinz, T. C. Berkelbach, A. Chernikov, Dielectric disorder in two-dimensional materials, *Nat. Nanotechnol.* **14**, 832–837 (2019).
4. T. G. Pedersen, S. Latini, K. S. Thygesen, H. Mera, B. K. Nikolić, Exciton ionization in multilayer transition-metal dichalcogenides, *New J. Phys.* **18**, 073043 (2016).
5. A. Taghizadeh, T. G. Pedersen, Nonlinear optical selection rules of excitons in monolayer transition metal dichalcogenides, *Phys. Rev. B* **99**, 235433 (2019).